Journal of
Polymer Materials

Tech Science Press

http://doi.org/10.32604/jpm.2026.087145

ARTICLE

Polydopamine-Coated Waste Cardboard Roll Evaporator for High-Performance Solar Desalination

Zheng Li[1,2], Xiaohan Li[2], Qiang Yin[3,*] and Jingkun Xu[1,*]

[1]School of Water Resources & Environmental Engineering, East China University of Technology, Nanchang, China
[2]Jiangxi Provincial Key Laboratory of Flexible Electronics, Flexible Electronics Innovation Institute, Jiangxi Science & Technology Normal University, Nanchang, China
[3]School of Chemistry and Materials Science, East China University of Technology, Nanchang, China
*Corresponding Authors: Qiang Yin. Email: sknyq@163.com; Jingkun Xu. Email: xujingkun1971@yeah.net

Received: 11 June 2026; Accepted: 02 September 2026; Published: 24 September 2026

ABSTRACT: Global freshwater scarcity has stimulated increasing interest in solar-driven interfacial evaporation for decentralized water purification. However, the development of low-cost evaporators that simultaneously achieve efficient photothermal conversion, continuous water supply, and functional separation of light harvesting and water transport remains a major challenge. Herein, we report a waste-cardboard-derived Janus cylindrical evaporator that integrates spatially separated photothermal conversion and water transport functions through a simple edge-immersion polydopamine (PDA) coating strategy followed by a rolling process. The PDA-coated upper region serves as a broad-band light absorber with a solar absorption exceeding 95% across 250–2500 nm and exhibits hydrophilicity, while the uncoated lower region retains the natural capillary network of cellulose fibers for continuous water supply. Under one-sun illumination, the evaporator delivers an evaporation rate of 2.07 kg m^{-2} h^{-1} with a photothermal conversion efficiency of 88.1%. In practical tests, it achieves over 99.9% rejection of primary ions (Na^+, Mg^{2+}, K^+, Ca^{2+}) and removes organic dyes with efficiencies exceeding 99%. This work presents a sustainable "waste-to-clean-water" strategy that valorizes discarded cardboard, offering a promising pathway toward decentralized and low-cost solar water purification.

KEYWORDS: Solar interfacial evaporation; waste cardboard; polydopamine; Janus evaporator; sea-water desalination

1 Introduction

Solar-driven interfacial evaporation has emerged as a highly promising technology for addressing global freshwater scarcity, offering a sustainable pathway for decentralized water purification powered entirely by renewable solar energy [1–3]. By localizing solar thermal energy at the air–water interface rather than heating the entire water body, this approach significantly improves energy utilization efficiency and minimizes heat loss [4–7]. Consequently, solar interfacial evaporation has attracted considerable attention for applications including seawater desalination, brackish water treatment, and wastewater purification, particularly in remote, off-grid, and resource-limited regions [8–11]. Despite substantial advances in photothermal materials and evaporator design, the practical implementation of this technology remains constrained by the challenge of simultaneously achieving low cost, facile fabrication, scalable production, efficient photothermal conversion, and continuous water supply within a single evaporator system.

In recent years, the valorization of waste biomass and discarded materials has attracted increasing attention as a sustainable strategy for evaporator fabrication [12–14]. Waste-derived substrates, including

wood residues, agricultural byproducts, and paper based materials, possess inherent advantages such as natural hydrophilicity, hierarchical porosity, and low thermal conductivity, which are favorable for capillary water transport and thermal localization during evaporation [15–18]. Recent reviews have highlighted various strategies to enhance solar desalination performance, including the use of wick materials with different configurations (e.g., floating, inclined, and corrugated) that can improve distiller productivity by 20–30%, as well as magnetic field-assisted systems that enhance evaporation and heat transfer efficiency [19,20]. Among these candidates, waste corrugated cardboard is particularly attractive because of its widespread availability, ultralow cost, and well-developed fibrous network composed of hydrophilic cellulose fibers rich in hydroxyl groups [21,22]. The interconnected porous structure of cardboard enables efficient capillary-driven water transport, making it a promising substrate for solar evaporation. However, its intrinsically low solar absorption severely limits direct photothermal utilization, necessitating the incorporation of an efficient light-harvesting layer. Hydrogel based materials have attracted considerable attention in diverse fields owing to their high water content, tunable porous structures, and excellent water retention capability [23–26]. In solar-driven water purification applications, these characteristics facilitate efficient water transport and interfacial evaporation, leading to remarkable desalination and contaminant removal performance [27,28]. Polydopamine (PDA), produced through the oxidative self-polymerization of dopamine under alkaline conditions, has emerged as a versatile photothermal coating owing to its broadband solar absorption, strong substrate adhesion, and excellent hydrophilicity [29–31]. Nevertheless, most reported PDA-based evaporators rely on full-immersion coating strategies that uniformly modify the entire substrate. Although such approaches enhance light absorption, they often compromise the intrinsic water transport capability of biomass substrates and fail to establish functional separation between photothermal conversion and water delivery. Furthermore, most PDA-coated evaporators are fabricated in planar configurations, which provide limited opportunities for enhancing light harvesting and vapor diffusion. Therefore, developing a simple and scalable evaporator that simultaneously enables functional separation, efficient water transport, enhanced light utilization, and effective vapor escape remains an important challenge.

Herein, we report a waste-cardboard-derived Janus cylindrical evaporator fabricated through a facile edge-immersion PDA coating strategy followed by a controlled rolling process. By selectively coating only the upper region of the cardboard, a spatially separated architecture is established in which the PDA-coated region serves as a highly efficient photothermal layer, while the uncoated region retains the native cellulose capillary network for continuous water transport. Subsequent rolling of the Janus sheet produces a three-dimensional cylindrical structure that promotes light trapping, thermal management, and vapor diffusion. The effects of PDA loading on optical absorption, surface wettability, and evaporation performance are systematically investigated. Under one-sun illumination, the optimized evaporator achieves an evaporation rate of 2.07 kg m^{-2} h^{-1} with a photothermal conversion efficiency of 88.1%. In addition, the evaporator exhibits excellent desalination capability with over 99.9% rejection of major seawater ions (Na^+, Mg^{2+}, K^+, and Ca^{2+}) and more than 99% removal efficiency toward representative organic dyes. This work provides a simple, low-cost, and scalable waste-to-clean-water strategy for transforming discarded corrugated cardboard into high-performance solar evaporators for sustainable water purification.

2 Materials and Methods

2.1 Materials

Dopamine hydrochloride (DA·HCl, 98%) was purchased from Aladdin (Shanghai, China). Sodium hydroxide (NaOH, AR, ≥96.0%, pellets) was obtained from General-Reagent. Hydrochloric acid (HCl, AR) was supplied by Keshi Reagent Co., Ltd. Commercial corrugated cardboard with a fluted core layer was

purchased from Alibaba and used as the substrate. The cardboard had a thickness of 0.306 cm and was cut into rectangular sheets with dimensions of 32 cm × 6 cm before use. Milli-Q purified water (18.2 MΩ cm) was employed throughout all experiments. All chemical reagents were used as received without further purification.

2.2 Fabrication of PDA-Coated Waste Cardboard Evaporators

PDA-coated waste cardboard roll evaporators were fabricated via an edge-immersion coating strategy followed by a controlled rolling process. Briefly, DA·HCl aqueous solutions with concentrations of 1.0 wt%, 1.5 wt%, 2.0 wt%, and 2.5 wt% were prepared by dissolving predetermined amounts of dopamine hydrochloride in a fixed volume of Milli-Q water. Separately, a NaOH aqueous solution was prepared at a concentration of 0.48 g mL^{-1}. Subsequently, 300 μL of the NaOH solution was added to the DA·HCl solution, and the mixture was allowed to oxidize at room temperature for 30 min under mild magnetic stirring, during which the solution gradually turned dark brown. The oxidation was then terminated by adding 300 μL of concentrated HCl, yielding a PDA coating suspension.

For the edge-immersion coating, the upper 2 cm region of each cardboard sheet (32 cm × 6 cm) was designated as the photothermal coating area. A volume of 2 mL of the prepared PDA coating suspension was uniformly applied onto this region for each coating cycle. The coating process was repeated five times at 30 min intervals to ensure sufficient PDA loading. After the final coating cycle, the samples were thoroughly rinsed three times with Milli-Q water to remove any loosely bound PDA aggregates and subsequently dried at 40°C for 12 h in a convection oven. The dried cardboard sheets exhibited a distinct "half-black, half-natural" appearance, with the upper 2 cm PDA-coated region showing a dark brown color and the lower 4 cm uncoated region retaining the original cardboard color.

The resulting Janus sheets were then rolled into cylindrical 3D evaporators. Rolling was initiated from the uncoated edge, ensuring that the PDA-coated region formed the upper portion of the cylinder while the uncoated region constituted the lower portion. This rolling protocol yielded a "black-top and natural-bottom" asymmetric cylindrical architecture. The rolled evaporators were placed upright in 100 mL beakers with a fixed diameter of 4.5 cm. The final evaporators had a height of 6 cm and a diameter matching the inner diameter of the beaker. Samples prepared from 1.0 wt%, 1.5 wt%, 2.0 wt%, and 2.5 wt% DA·HCl solutions were denoted as PDA-1.0, PDA-1.5, PDA-2.0, and PDA-2.5, respectively. Unless otherwise specified, subsequent characterization and performance tests were conducted on the optimized sample. The actual amount of PDA deposited was quantified by measuring the dry weight of the cardboard sheets before and after coating using an analytical balance. The mass gain per unit area (mg cm^{-2}) was calculated for each dopamine concentration.

2.3 Materials Characterization

The surface morphology and microstructure of the raw cardboard and PDA-coated samples were examined using field-emission scanning electron microscopy (FE-SEM). Prior to imaging, all samples were sputter-coated with a thin layer of gold to minimize charging effects. Cross-sectional SEM images were obtained by cutting the samples with a sharp blade to expose the coating boundary. Energy-dispersive X-ray spectroscopy (EDS) mapping was performed on the same SEM instrument to analyze the elemental distribution of carbon (C), oxygen (O), and nitrogen (N) across the coating interface.

The optical absorption properties of the samples in the ultraviolet-visible-near-infrared (UV-Vis-NIR) range (300–2500 nm) were measured using a UV-Vis-NIR spectrophotometer equipped with an integrating

sphere. The solar-weighted absorption (α) was calculated based on the measured reflectance (R) and transmittance (T) spectra using.

$$A = 1 - T - R$$

Water contact angle measurements were performed on a contact angle goniometer at ambient temperature. A droplet of Milli-Q water (approximately 5 μL) was deposited onto the sample surface, and the dynamic spreading behavior was recorded. Static contact angles were determined from the captured images using the built-in software.

2.4 Characterization of PDA-Coated Waste Cardboard Evaporators

Solar-driven interfacial evaporation experiments were conducted using a solar simulator equipped with an air mass 1.5 global (AM 1.5G) optical filter. The light intensity was calibrated to 1 kW m^{-2} (1 sun) using an optical power meter before each test. The PDA-coated cardboard roll evaporator was placed upright in a 100 mL beaker containing simulated seawater (3.5 wt% NaCl aqueous solution) or other test solutions. The beaker was placed on an electronic analytical balance to monitor the real-time mass change due to water evaporation. The mass data was recorded via a computer interface.

The surface temperature of the evaporator under illumination was monitored using an infrared thermal camera. All evaporation tests were conducted at an ambient temperature of approximately 25°C and a relative humidity of approximately 50%. Before each test, the system was allowed to stabilize for 30 min under dark conditions to eliminate any initial thermal or moisture fluctuations.

The evaporation rate (kg m^{-2} h^{-1}) was calculated from the slope of the mass loss curve during the steady-state evaporation phase [32–34].

$$m_g = \frac{d_m}{(S * d_t)}$$

where Δm is the mass change (kg), A is the projected evaporation area (m^2), and Δt is the time interval (h). The projected area of the cylindrical evaporator was taken as the cross-sectional area of the beaker ($A = \pi \times (d/2)^2$, where d = 4.5 cm). This approach follows the standard practice established in the field of interfacial solar evaporation, where the evaporation rate is normalized to the projected area of the evaporator [35–37]. as it represents the effective solar interception area and the primary evaporation interface.

Outdoor solar evaporation experiments were carried out on a sunny day (04 July 2026) from 8:00 to 18:00 in Nanchang, China. The PDA-WCE was placed upright in a 100 mL beaker containing 3.5 wt% NaCl solution, and the beaker was placed on an electronic balance. Mass loss was recorded at 1 h intervals to calculate the evaporation rate and cumulative water collection. Simultaneously, the solar intensity was monitored using an optical power meter (CEL-NP2000-2A).

2.5 Solar Desalination and Water Purification Performance

The desalination performance was evaluated using simulated seawater (3.5 wt% NaCl) and NaCl solutions of varying concentrations (0, 3.5, 10, and 20 wt%). During the evaporation test, the generated water vapor was condensed and collected using a custom-built condensation cover. The concentrations of primary ions (Na^+, Mg^{2+}, K^+, Ca^{2+}) in the original feed solution and the collected condensed water were measured using inductively coupled plasma optical emission spectroscopy (ICP-OES).

For organic dye removal tests, aqueous solutions of methylene blue (MB), methyl orange (MO), and rhodamine B (RhB) were prepared at concentrations of 5 mg L^{-1} and used as model wastewater. The UV-Vis absorption spectra of the feed solutions and the collected purified water were recorded on a UV-Vis spectrophotometer. The dye removal efficiency was calculated from the decrease in absorbance at the characteristic absorption peak of each dye.

The cycling stability of the evaporator was evaluated by conducting evaporation tests for 10 cycles under 1 sun illumination. Each cycle consisted of 60 min of illumination followed by 30 min of dark equilibration. After cycling, the evaporator was visually inspected for salt accumulation and structural integrity.

3 Results and Discussion

3.1 Material Design, Preparation of Polydopamine-Coated Waste Cardboard Evaporator (PDA-WCE)

Fig. 1 illustrates the design concept, fabrication process, and working principle of the polydopamine-coated waste cardboard evaporator (PDA-WCE). Waste corrugated cardboard is selected as the substrate because of its widespread availability, ultralow cost, and interconnected cellulose-fiber network, which provides efficient capillary-driven water transport. These characteristics make waste cardboard an attractive candidate for developing sustainable solar evaporators while simultaneously promoting waste valorization.

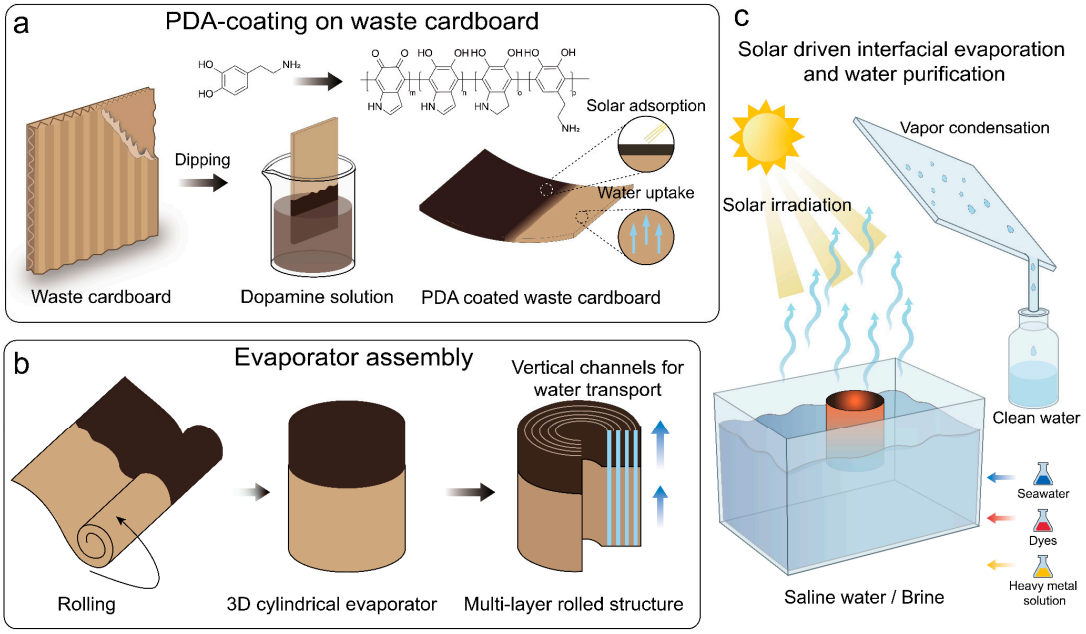

Figure 1: Schematic illustration of the PDA-coated waste cardboard roll evaporator. (**a**) Edge-immersion PDA coating to obtain a Janus sheet. (**b**) Rolling from the uncoated edge to form a "black-top and natural-bottom" cylindrical evaporator. (**c**) Solar-driven interfacial evaporation for clean water production.

To integrate efficient solar absorption with continuous water supply, Janus architecture is constructed through a simple edge-immersion PDA coating strategy. As illustrated in Fig. 1a, only the upper portion of the cardboard sheet is immersed in the dopamine solution, producing a partially coated structure with distinct photothermal and water-transport regions [38,39]. The PDA-coated upper region is designed to serve as the primary solar-absorbing layer, whereas the uncoated lower region retains the native cellulose network

for continuous water delivery [30]. Such spatial separation of functions is expected to reduce interference between photothermal conversion and water transport, thereby improving overall evaporation performance.

Following the selective coating process, the Janus sheet is rolled from the uncoated edge to form a cylindrical evaporator with a multilayer architecture (Fig. 1b). Compared with conventional planar configurations, the rolled structure provides a larger effective evaporation interface and generates multiple internal reflection pathways for enhanced light utilization. Meanwhile, the vertically aligned channels formed between adjacent layers facilitate rapid capillary water transport and promote vapor diffusion during operation.

The working mechanism of PDA-WCE is schematically illustrated in Fig. 1c. Under solar irradiation, the PDA-coated region absorbs incident light and converts it into thermal energy, generating localized heating at the evaporation surface. Water is continuously supplied from the bulk reservoir through the uncoated cellulose network and transported upward to the evaporation interface via capillary action. The generated vapor subsequently diffuses into the surrounding atmosphere or condenses on a collection surface for freshwater production. Through the synergistic integration of functional separation and three-dimensional structural design, the PDA-WCE provides a simple and scalable platform for efficient solar-driven water purification.

3.2 Morphological Characteristics and Water Transport Behavior of PDA-WCE

Fig. 2 presents the coating mechanism, morphological characteristics, and water transport behavior of PDA-WCE. As illustrated in Fig. 2a, dopamine molecules undergo oxidative self-polymerization under alkaline conditions, forming a PDA coating on the cardboard surface. The coating is firmly anchored to the cellulose substrate through hydrogen-bonding interactions and π–π stacking, providing a stable photothermal layer for subsequent solar evaporation [40,41].

The surface morphology of PDA-WCE is investigated by SEM. As shown in Fig. 2b, the pristine cardboard consists of an interconnected network of cellulose fibers with abundant pores and channels. Such a hierarchical porous structure is beneficial for capillary-driven water transport. After PDA modification, granular deposits can be clearly observed on the fiber surfaces, indicating the successful formation of a PDA coating layer. Importantly, the overall porous framework of the cardboard remains well preserved after coating, suggesting that the water transport pathways are largely maintained. Water contact angle measurements show that the uncoated cardboard region exhibits better hydrophilicity than the PDA-coated region (Fig. S1). This contrast in wettability supports the Janus design, in which the uncoated region facilitates rapid water transport while the coated region serves as the photothermal layer. To validate the structural advantage of the Janus design, a fully PDA-coated cardboard is tested as a control. SEM observations reveal that full coating severely clogs the internal micro-capillaries, which restricts the dynamic water transport speed to 0.045 g s^{-1} (Figs. S2 and S3). In contrast, the selective edge-coating of the Janus evaporator leaves the bottom water-supply region uncoated, preserving the open porous network to ensure a rapid liquid transport of 0.085 g s^{-1}.

Efficient water supply is essential for sustaining continuous solar evaporation. Therefore, the capillary water transport behavior of PDA-WCE is evaluated, as illustrated in Fig. 2d,e. Owing to the hydrophilic cellulose network and interconnected porous structure, water rapidly migrates upward through capillary action. The waterfront reaches approximately 121 mm after 60 s and further increases to 196 mm after 120 s. Such rapid water transport demonstrates the excellent water replenishment capability of the PDA-WCE, ensuring a continuous supply of water to the evaporation interface during operation [42,43].

The elemental mapping results shown in Fig. 2c further reveal the presence and distribution of characteristic elements on the sample surface. The observed elemental signals confirm the successful incorporation and retention of the functional coating while maintaining the structural integrity of the

substrate. Cross-sectional SEM imaging further reveals a distinct boundary between the PDA-coated and uncoated regions, directly confirming the spatially separated Janus architecture (Fig. S2). Overall, the combination of the preserved porous network and strong capillary transport provides a favorable foundation for efficient solar-driven interfacial evaporation.

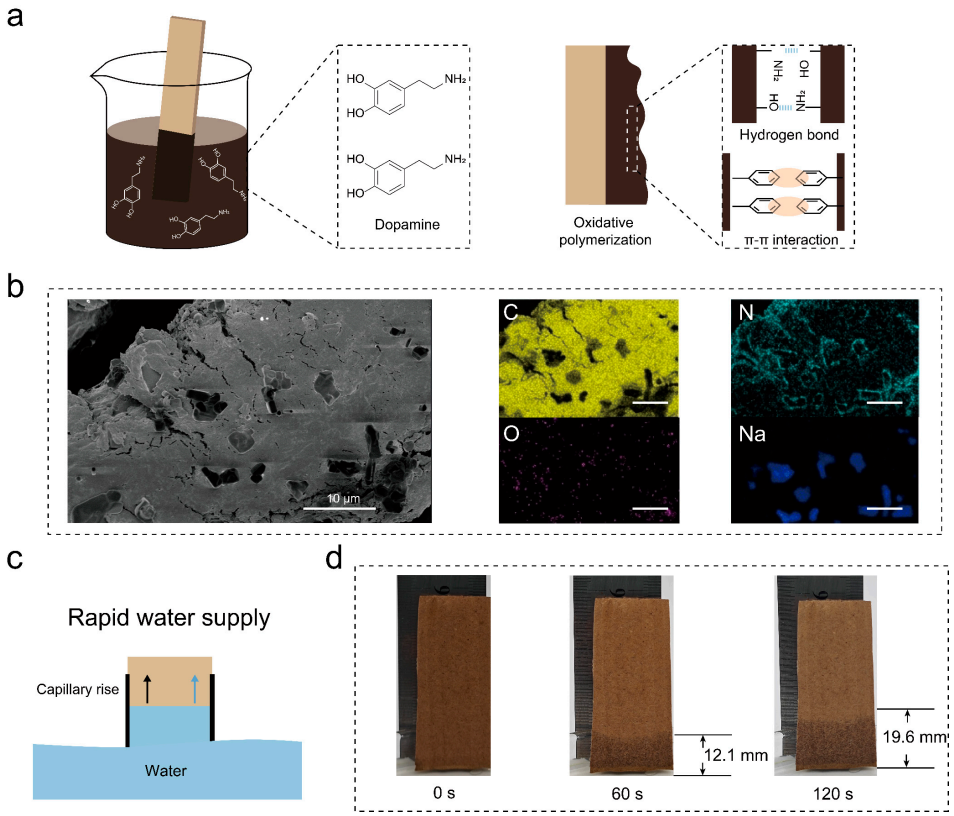

Figure 2: Morphological characteristics and water transport behavior of PDA-WCE. (**a**) Schematic illustration of the oxidative self-polymerization of dopamine and the formation mechanism of the PDA coating on the cardboard surface through hydrogen-bonding and π–π interactions; (**b**) SEM images of PDA-WCE showing the interconnected cellulose fiber network and PDA deposition on the fiber surfaces, and EDS elemental mapping images displaying the spatial distribution of C, N, O, and Na elements; (**c**) Schematic illustration of capillary-driven water transport within the porous cellulose network of PDA-WCE; (**d**) Dynamic water-rise photographs demonstrating the capillary water transport behavior of PDA-WCE at different time intervals.

3.3 Sunlight Absorption and Photothermal Conversion of PDA-WCE

Fig. 3 illustrates the optical absorption characteristics and photothermal conversion performance of PDA-WCE. As schematically shown in Fig. 3a, the rolled multilayer architecture generates multiple internal reflection pathways within the cylindrical structure, which effectively prolong the optical path length and enhance solar energy utilization. Such a three-dimensional configuration is expected to improve light harvesting compared with conventional planar evaporators.

The optical absorption properties of PDA-WCE samples prepared using different dopamine concentrations were evaluated by UV–Vis–NIR spectroscopy (Fig. 3b). Pristine cardboard exhibited relatively low absorption across the solar spectrum, with an average absorptance of approximately 75%. After PDA modification, the absorption intensity increased significantly over the entire wavelength range of 250–2500 nm. As the dopamine concentration increased from 1.0 to 2.0 wt%, the average solar absorptance gradually increased, reaching

approximately 93.7% (Fig. 3c). A further increase in the dopamine concentration to 2.5 wt% resulted in only a negligible improvement in solar absorptance, suggesting that the surface coverage or effective optical contribution of PDA had approached a plateau. The enhanced light absorption can be attributed to the broadband optical response of PDA arising from its heterogeneous conjugated structure containing catechol, quinone, and indole-related units.

The photothermal conversion capability of PDA-WCE is subsequently investigated under solar irradiation. As shown in Fig. 3d, the surface temperature increases rapidly from 36.5°C to 50.7°C within the first 20 min and then remains relatively stable, demonstrating efficient solar-to-thermal energy conversion and favorable thermal localization. The influence of light intensity on surface temperature is presented in Fig. 3e. The equilibrium temperature increases progressively with increasing solar intensity, reaching approximately 54, 55, 60, and 70°C under 0.5, 1.0, 1.5, and 2.0 sun illumination, respectively. Moreover, all samples exhibit a rapid thermal response and reached a quasi-steady state within approximately 10 min. These results demonstrate that the combination of broadband solar absorption and rolled architecture endows PDA-WCE with excellent photothermal conversion capability, providing a solid foundation for efficient solar-driven interfacial evaporation.

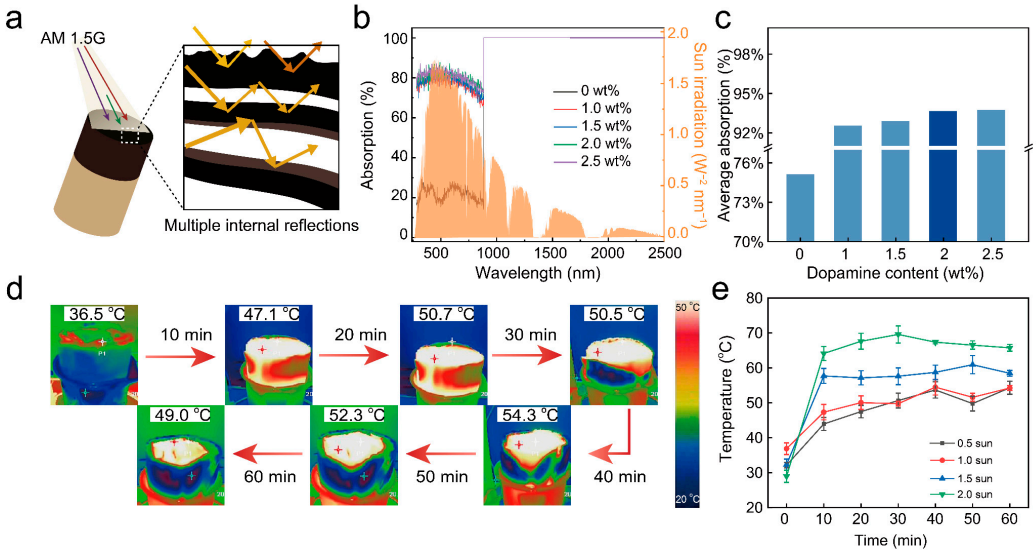

Figure 3: Sunlight absorption and photothermal conversion performance of PDA-WCE. (**a**) Schematic illustration of the enhanced light-harvesting mechanism of the rolled PDA-WCE through multiple internal reflections; (**b**) UV–Vis–NIR absorption spectra of PDA-WCE prepared with different dopamine concentrations in the wavelength range of 250–2500 nm; (**c**) Average solar absorptance of PDA-WCE with different dopamine concentrations; (**d**) Infrared thermal images and corresponding surface temperature evolution of PDA-WCE under one-sun illumination; (**e**) Surface temperature variation of PDA-WCE under different solar intensities (0.5, 1.0, 1.5, and 2.0 sun).

3.4 Solar-Driven Evaporation Performance of PDA-WCE

The solar-driven evaporation performance of PDA-WCE is systematically evaluated under controlled laboratory conditions (Fig. 4a). The experimental setup consists of a solar simulator, an electronic balance for mass measurement, saline samples, and infrared (IR) imaging to monitor temperature distribution, ensuring accurate assessment of photothermal conversion efficiency. The effect of polydopamine (PDA) coating concentration on evaporation is first investigated (Fig. 4b,c). Mass loss curves reveal that the 2 wt% PDA-WCE achieves the highest water evaporation among the tested concentrations. At lower concentrations (1 wt%),

photothermal absorption is insufficient, whereas higher concentrations (>2 wt%) lead to excessive PDA deposition, partially blocking the capillary channels and slightly reducing water transport. The optimized evaporator is prepared using 2.0 wt% PDA solution with five coating cycles (Fig. S4). This limitation is further proved by the fully coated control group. Due to the clogged capillaries restricting the water supply, the fully coated sample only exhibits an evaporation rate of 1.59 kg m^{-2} h^{-1}. Conversely, by successfully maintaining unobstructed water delivery, the 2 wt% Janus sample achieves a peak evaporation rate of 2.07 kg m^{-2} h^{-1}.

To verify the advantage of the Janus architecture, the evaporation performances of the uncoated waste cardboard evaporator (WCE), the fully PDA-coated evaporator (f-PDA-WCE), and the Janus PDA-WCE were evaluated under 1 sun illumination. As shown in Fig. S3, the pristine WCE exhibited a relatively low evaporation rate of 1.35 kg m^{-2} h^{-1} because of its limited solar absorption (Fig. S5). After full PDA coating, the f-PDA-WCE achieved a higher evaporation rate of 1.59 kg m^{-2} h^{-1} owing to its enhanced photothermal conversion. However, complete PDA coverage of the cellulose network significantly reduced the capillary water transport rate (Fig. S3). In contrast, the Janus PDA-WCE delivered a substantially higher evaporation rate of 2.07 kg m^{-2} h^{-1}, demonstrating that the uncoated lower region preserved efficient water supply, while the PDA-coated upper region provided strong solar absorption.

The influence of solar intensity on the evaporation performance was subsequently investigated (Fig. 4d,e). The evaporation rate shows a positive correlation with light intensity, ranging from 0.5 to 2 suns. Mass loss increases rapidly at higher intensities, reaching 4.45 kg m^{-2} h^{-1} under 2 suns, indicating that PDA-WCE effectively converts incident solar energy into thermal energy and achieves rapid thermal equilibrium across varying irradiation conditions. To understand the energy requirement of water evaporation, the equivalent evaporation enthalpy (ΔHequ) is determined (Fig. 4f). The 2 wt% PDA-WCE exhibits a ΔHequ of approximately 1524 J g^{-1}, significantly lower than that of pure water (2440 J g^{-1}). To experimentally verify the water states responsible for this reduction, Raman spectroscopy is conducted on the water-wetted samples (Fig. S6). By deconvoluting the O–H stretching vibration bands, the states of the water clusters are quantitatively analyzed. The results reveal a significant presence of intermediate water, with the ratio of intermediate water (IW) to free water (FW) reaching approximately 1.43:1. This indicates that the abundant hydrophilic functional groups in the PDA layer (such as catechol and amine groups) form hydrogen bonds with adjacent water molecules, thereby weakening the inherent hydrogen-bonding network of bulk water. This reduction is attributed to the synergistic effect of intermediate and bound water states in the PDA layer, which facilitates water transport and reduces the energy needed for phase change.

The long-term operational stability of the PDA-WCE is evaluated through extended cycling tests under both pure water and high-salinity conditions. In pure water, the evaporator is subjected to 60 consecutive cycles under 1 sun illumination (60 min per cycle). As shown in Fig. 4g, the evaporation rate exhibits natural fluctuations but remains generally stable throughout the test, decreasing from an initial average of 2.09 kg m^{-2} h^{-1} to 1.86 kg m^{-2} h^{-1} after 60 cycles, corresponding to a total decline of only approximately 10%. Correspondingly, the solar-to-vapor energy conversion efficiency reaches approximately 88.1% for the 2 wt% PDA sample (Fig. 4h), consistent with the trend observed for evaporation rates. To evaluate the long-term stability of the material in practical applications, a continuous 50-cycle evaporation test is conducted using 20 wt% high-salinity brine under 1 sun irradiation (Fig. S7). The results show that the initial evaporation rate is 2.01 kg m^{-2} h^{-1}, and it decreases to 1.66 kg m^{-2} h^{-1} after 50 cycles, with an overall performance decay of only 21%. Furthermore, we monitor the time-dependent morphological changes of salt crystallization at the evaporation interface (Fig. S8). It can be intuitively observed that the salt crystals initially accumulate on the surface gradually dissolve over time during the evaporation process.

Finally, the performance of PDA-WCE is benchmarked against other reported solar evaporators (Fig. 4i). The comparison demonstrates that PDA-WCE exhibits competitive evaporation rates and energy efficiencies, positioning it among the top-performing biomass-derived photothermal materials in literature [44–47]. The results highlight that optimized PDA coating, effective light absorption, and rapid water transport synergistically enhance the solar evaporation capability of PDA-WCE.

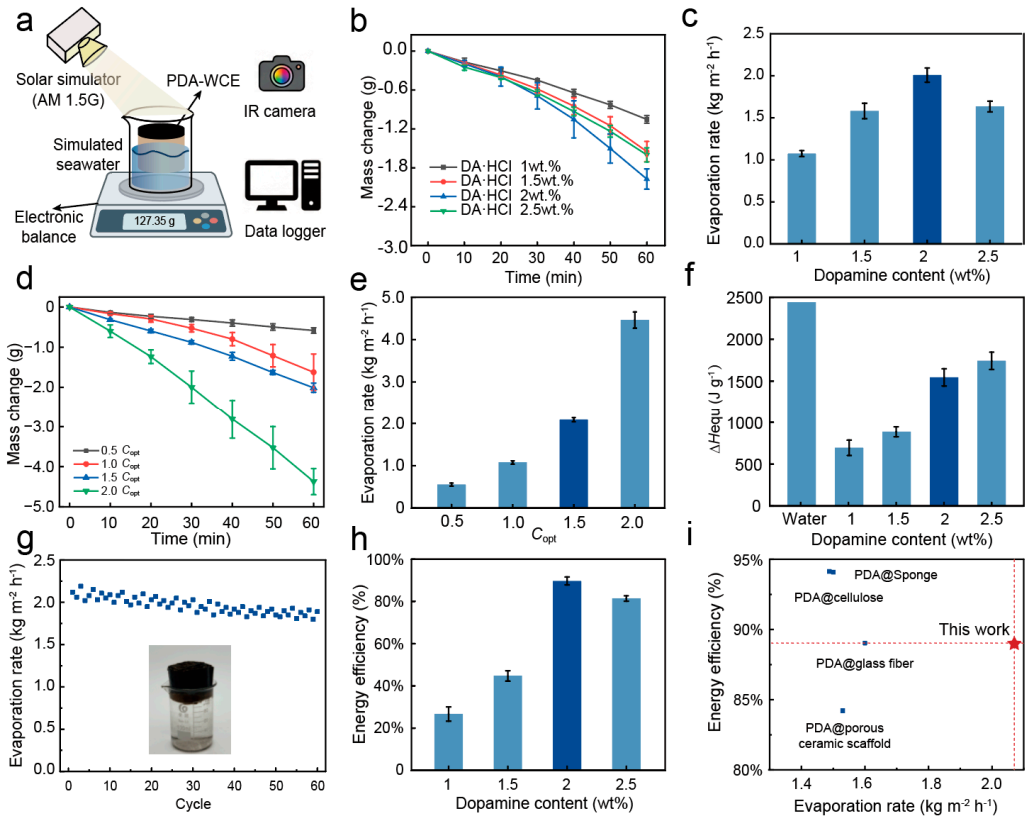

Figure 4: Solar-driven evaporation performance of PDA-WCE. (**a**) Schematic illustration of the experimental setup for solar evaporation measurements; (**b**) Mass change curves of PDA-WCE prepared with different dopamine concentrations under one-sun illumination; (**c**) Corresponding evaporation rates of PDA-WCE with different dopamine concentrations; (**d**) Mass change curves of the optimized PDA-WCE under different solar intensities; (**e**) Corresponding evaporation rates under different solar intensities; (**f**) Equivalent evaporation enthalpy (ΔHequ) of water and PDA-WCE samples with different dopamine concentrations; (**g**) Cycling stability of the optimized PDA-WCE over 60 consecutive evaporation cycles; (**h**) Energy conversion efficiencies of PDA-WCE prepared with different dopamine concentrations; (**i**) Comparison of evaporation rate and energy efficiency between this work and previously reported solar evaporators.

3.5 Water Purification and Desalination Performance of PDA-WCE

The solar-driven water purification system is constructed using a PDA-WCE evaporator paired with a condensation collector to harvest freshwater (Fig. 5a). This setup enables quantitative evaluation of the system's ability to remove organic dyes, dissolved salts, and heavy metal ions under controlled laboratory conditions. The efficiency of PDA-WCE in removing organic dyes is assessed using Rhodamine B (RhB) and Methylene Blue (MB) solutions. Visual inspection reveals complete decolorization of the collected water, indicating that the dyes are fully rejected by the evaporation-condensation process (Fig. 5b). UV–Vis absorption spectra confirm the disappearance of characteristic peaks at 554 nm for RhB and 664 nm for MB

(Fig. 5c), demonstrating near 100% removal efficiency. These results confirm that nonvolatile dye molecules remain in the feed solution while only pure water vapor is transported and condensed.

PDA-WCE is further evaluated for desalination using NaCl solutions with varying salinities, including seawater-level salinity (~3.5%), concentrated brine (~10%), and highly concentrated brine (~25%). The collected freshwater exhibits dramatically reduced salinity (≈0.001–0.1‰), well below the drinking water standards defined by United States Environmental Protection Agency (EPA) and World Health Organization (WHO) (Fig. 5d). Major ions (Na^+, K^+, Ca^{2+}, and Mg^{2+}) are reduced to 0.01–0.05 mg L^{-1}, corresponding to an ion rejection efficiency of approximately 99.9% (Fig. 5e). These findings indicate that dissolved salts are effectively retained in the bulk solution due to their nonvolatile nature, while water vapor is selectively transported and condensed.

Industrial wastewater containing Mn^{2+}, Cr^{3+}, Cu^{2+}, and Ni^{2+} is treated with PDA-WCE. The concentrations of these heavy metal ions decrease from 30–40 mg L^{-1} to 0.3–0.7 mg L^{-1} in the collected freshwater, achieving removal rates exceeding 98% (Fig. 5f). This demonstrates the system's applicability for heavy metal-contaminated water, highlighting its versatility beyond conventional seawater desalination.

To evaluate the practical viability of the PDA-WCE under real-world conditions, an outdoor evaporation test is performed on a sunny day (04 July 2026) in Nanchang, China, from 08:00 to 18:00. The solar intensity and mass loss are recorded at 1 h intervals (Fig. S9). The solar intensity increases from 420 W m^{-2} at 08:00 to a peak of 960 W m^{-2} at 12:00. The evaporation rate exhibits a synchronous variation with the solar intensity, rising from 0.08 kg m^{-2} h^{-1} in the early morning to a maximum of 0.40 kg m^{-2} h^{-1} around noon and declining thereafter. The cumulative water collection over the 11 h period reaches 1.72 L m^{-2}. These results demonstrate the preliminary outdoor feasibility of the PDA-coated waste cardboard roll evaporator, indicating its potential for practical decentralized solar desalination.

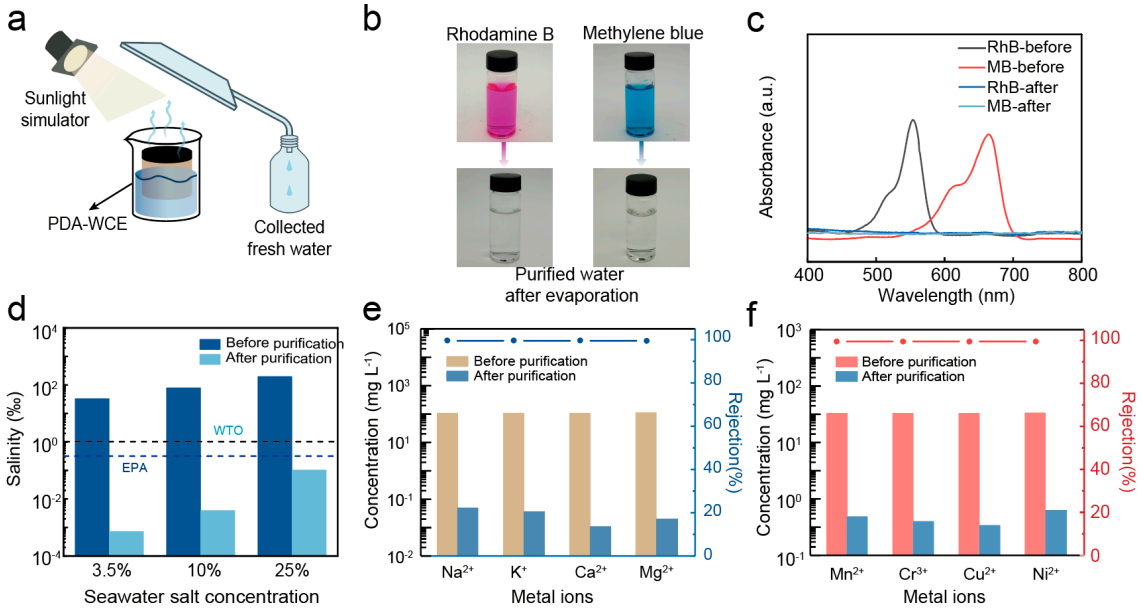

Figure 5: Water purification and desalination performance of PDA-WCE. (**a**) Schematic illustration of the solar-driven water purification setup; (**b**) Photographs of rhodamine B (RhB) and methylene blue (MB) solutions before and after purification; (**c**) UV–Vis absorption spectra of RhB and MB solutions before and after purification; (**d**) Salinity of simulated seawater, Bohai Sea water, and Dead Sea water before and after purification, compared with EPA and WHO drinking water standards; (**e**) Concentrations and rejection efficiencies of major seawater ions (Na^+, K^+, Ca^{2+}, and Mg^{2+}) before and after purification; (**f**) Concentrations and rejection efficiencies of heavy metal ions (Mn^{2+}, Cr^{3+}, Cu^{2+}, and Ni^{2+}) before and after purification.

4 Conclusion

In this work, we have demonstrated a waste-cardboard-derived Janus cylindrical evaporator that combines efficient photothermal conversion with continuous water transport through a simple edge-immersion polydopamine (PDA) coating and rolling process. Unlike conventional full-surface PDA evaporators, the selective edge coating preserves the intrinsic capillary network in the uncoated region, achieving functional separation between light harvesting and water delivery. The cylindrical Janus architecture further enhances light absorption and facilitates vapor escape, enabling a high evaporation rate of 2.07 kg m^{-2} h^{-1} with a solar-to-vapor conversion efficiency of 88.1% under one-sun irradiation. In addition, the evaporator effectively removes primary ions and organic dyes with efficiencies exceeding 99%, demonstrating its potential for practical water purification. Importantly, outdoor tests under natural sunlight demonstrate a daily water collection of 1.72 L m^{-2} d^{-1}, demonstrating the preliminary outdoor feasibility of this low-cost Janus evaporator under real environmental conditions. This study highlights a sustainable "waste-to-clean-water" strategy that valorizes discarded cardboard and introduces a simple yet scalable design principle for interfacial evaporators, offering distinct advantages in terms of material accessibility, structural functionality, and operational efficiency compared with previously reported systems.

Acknowledgement: We express our heartfelt gratitude to Prof. Baoyang Lu (Jiangxi Science and Technology Normal University) for valuable discussions. We also extend our thanks to Jiayi Li and Ziyang Qiu for their invaluable assistance throughout the course of this research. We would also like to thank Dr. Sanmei Liu at the Analytical & Testing Center of Jiangxi Science &Technology Normal University for the help on SEM imaging.

Funding Statement: This research was financially supported by National Natural Science Foundation of China (52373184 and U24A2066) and the Jiangxi Provincial Key Laboratory of Flexible Electronics (20242BCC32010).

Author Contributions: The authors confirm contribution to the paper as follows: study conception and design: Zheng Li, Jingkun Xu; methodology: Zheng Li, Xiaohan Li; data collection: Zheng Li, Xiaohan Li; analysis and interpretation of results: Zheng Li, Qiang Yin, Jingkun Xu; software: Zheng Li, Qiang Yin; investigation: Zheng Li, Xiaohan Li; visualization: Xiaohan Li; writing—original draft: Zheng Li; writing—review & editing: Zheng Li, Qiang Yin, Jingkun Xu; supervision: Qiang Yin, Jingkun Xu; funding acquisition: Jingkun Xu. All authors reviewed and approved the final version of the manuscript.

Availability of Data and Materials: All data generated or analyzed during this study are included in this published article.

Ethics Approval: Not applicable.

Conflicts of Interest: The authors declare no conflicts of interest.

Supplementary Materials: The supplementary material is available online at https://www.techscience.com/doi/10.32604/jpm.2026.087145/s1.

References

1. Zou H, Xu X, Yao M, Lu B. Conjugated polymer hydrogel: A highly efficient material of solar water purification. J Polym Mater. 2025;42(2):339–58. [CrossRef].
2. Tao P, Ni G, Song C, Shang W, Wu J, Zhu J, et al. Solar-driven interfacial evaporation. Nat Energy. 2018;3(12):1031–41. [CrossRef].
3. Mo H, Wang Y. A bionic solar-driven interfacial evaporation system with a photothermal-photocatalytic hydrogel for VOC removal during solar distillation. Water Res. 2022;226:119276. [CrossRef].
4. Li X, Min X, Li J, Xu N, Zhu P, Zhu B, et al. Storage and recycling of interfacial solar steam enthalpy. Joule. 2018;2(11):2477–84. [CrossRef].

5. Chen Y, Shen L, Qi Z, Luo Z, Li X, Bao H. Large-scale implementation of solar interfacial desalination. Nat Sustain. 2025;8(2):162–9. [CrossRef].
6. Yao J, Zhong Q, Zhang J, Zhao J, Wang Z. Interfacial solar evaporation for zero liquid discharge desalination. Commun Mater. 2024;5:103. [CrossRef].
7. Wu X, Lu Y, Ren X, Wu P, Chu D, Yang X, et al. Interfacial solar evaporation: From fundamental research to applications. Adv Mater. 2024;36(23):2313090. [CrossRef].
8. Wang M, Wei Y, Wang X, Li R, Zhang S, Wang K, et al. An integrated system with functions of solar desalination, power generation and crop irrigation. Nat Water. 2023;1(8):716–24. [CrossRef].
9. Zhou Y, Wang Z, Chen X, Ji J, Zhang L, Meng C. Advancing robust all-weather desalination: A critical review of emerging photothermal evaporators and hybrid systems. Commun Mater. 2025;6:29. [CrossRef].
10. Xu J, Wang Z, Chang C, Fu B, Tao P, Song C, et al. Solar-driven interfacial desalination for simultaneous freshwater and salt generation. Desalination. 2020;484:114423. [CrossRef].
11. Gao H, Bing N, Bao Z, Xie H, Yu W. Sandwich-structured MXene/wood aerogel with waste heat utilization for continuous desalination. Chem Eng J. 2023;454:140362. [CrossRef].
12. Guo Y, Lu H, Zhao F, Zhou X, Shi W, Yu G. Biomass-derived hybrid hydrogel evaporators for cost-effective solar water purification. Adv Mater. 2020;32(11):e1907061. [CrossRef].
13. Ma W, Cao W, Cui M, Lu H, Xiong R, Huang C. Biomass-derived 3D evaporator with antifouling and salt-rejecting toward solar-enabled steam generation, desalination, and electricity generation. Chem Eng J. 2023;478:147404. [CrossRef].
14. Wilson HM, Hossain MN, Raheman SRA, Lee SJ. All-day desalination and ZLD-oriented brine production using a grass biomass pellet-derived biochar–carbon fabric evaporator. Chem Eng J. 2025;519:165432. [CrossRef].
15. Ren Y, Zhou R, Dong TG, Lu Q. Wood-inspired polypyrrole/cellulose aerogels with vertically aligned channels prepared by facile freeze-casting for efficient interfacial solar evaporation. J Mater Chem A. 2023;11(33):17748–58. [CrossRef].
16. Pang Y, Chu X, Song L, Jin L, Ma C, Wu Y, et al. Laser-engraved wood-based evaporators: A sustainable approach for solar interfacial evaporation. Chem Eng J. 2024;479:147891. [CrossRef].
17. Sun Y, Zhuo M, Yuan X, Chen W, Zhang J, Liu W, et al. Construction of high-performance hydrogel-wood solar evaporator for desalination and water treatment through structural engineering design. Chem Eng J. 2025;522:167095. [CrossRef].
18. Pan Z, Zhang H, Liang J, Qi Z, Wang J, Ding M, et al. Efficient fabrication of cellulose-based hydrogels for effective heavy metal ion adsorption from oral medical wastewater. Int J Biol Macromol. 2026;370:152880. [CrossRef].
19. Hussein AK, Gharsallah S, Ali Kadhim S, El Hadi Attia M, Rasul MK, Homod RZ, et al. Magnetic-field-enhanced solar desalination: A comprehensive review of advanced configurations and performance improvements. Heat Trans. 2026;55(3):2150–73. [CrossRef].
20. Rashid FL, Al-Obaidi MA, Hammoodi KA, Mahdi AJ, Ali Kadhim S, Chaichan MT, et al. Innovations and ongoing advancements of the wick type solar still: A review. Results Eng. 2024;24:103049. [CrossRef].
21. Zhao Q, Liu J, Wu Z, Xu X, Ma H, Hou J, et al. Robust PEDOT: PSS-based hydrogel for highly efficient interfacial solar water purification. Chem Eng J. 2022;442:136284. [CrossRef].
22. Zhao Q, Wu Z, Xu X, Yang R, Ma H, Xu Q, et al. Design of poly(3,4-ethylenedioxythiophene): Polystyrene sulfonate-polyacrylamide dual network hydrogel for long-term stable, highly efficient solar steam generation. Sep Purif Technol. 2022;300:121889. [CrossRef].
23. Zhao Y, Ma X, Wu Z, Amjad M, Wen D. Synergistic solar interfacial evaporation and photocatalysis enabled by a hierarchical porous hydrogel reactor. Adv Funct Mater. 2026;36(65):e77086. [CrossRef].
24. Wang L, Wang W, Wan R, Yao M, Chen W, Zhang L, et al. All 3D-printed high-sensitivity adaptive hydrogel strain sensor for accurate plant growth monitoring. Soft Sci. 2025;5:2. [CrossRef].
25. Wang F, Xue Y, Wang Y, Wang Q, Wen P, Chen X, et al. Multimodal hydrogel bioelectronics for closed-loop diagnosis and treatment of cardiac diseases. Adv Funct Mater. 2026;36(47):e27184. [CrossRef].
26. Li J, Teng J, Jia X, Lin Y, Zhang L, Li H, et al. A superbranched multi-armed crosslinking strategy for robust conducting polymer hydrogels toward wearable sensing and encrypted communication. Wearable Electron. 2026;3:93–102. [CrossRef].

27. Li Z, Qiu Z, Xu J, Lu B. High-performance ferroferric oxide nanocomposite hydrogel for integrated evaporative desalination-crop irrigation bifunctional system toward scalable seawater agriculture. Chem Eng J. 2025;525:169656. [CrossRef].
28. Li Z, Yao MT, Qiu ZY, Xu JK, Lu BY. Fe^{3+}-coordinated dual-crosslinked conjugated polymer hydrogels with ultrahigh evaporation rate for efficient desalination and sustainable agriculture. Chin J Polym Sci. 2026;44(3):632–43. [CrossRef].
29. Chong W, Meng R, Liu Z, Liu Q, Hu J, Zhu B, et al. Superhydrophilic polydopamine-modified carbon-fiber membrane with rapid seawater-transferring ability for constructing efficient hanging-model evaporator. Adv Fiber Mater. 2023;5(3):1063–75. [CrossRef].
30. Zhao Z, Wang J, Yu S, Zhang X. Wood aerogel based on PDA-modified rGO mimicking mussel mucin for efficient interfacial evaporation. Desalination. 2024;591:118013. [CrossRef].
31. Su Q, Yan J, Xiao W, Liu Y, Li L, Wang J, et al. Flexible nanofiber composite solar evaporator for simultaneous interfacial evaporation and heavy metal ion adsorption. Chem Eng J. 2024;490:151814. [CrossRef].
32. Yang HC, Lu F, Li HN, Zhang C, Darling SB, Xu ZK. Membranes in solar-driven evaporation: Design principles and applications. Adv Funct Mater. 2023;33(43):2304580. [CrossRef].
33. Hou L, Li S, Qi Y, Liu J, Cui Z, Liu X, et al. Advancing efficiency in solar-driven interfacial evaporation: Strategies and applications. ACS Nano. 2025;19(10):9636–83. [CrossRef].
34. Zhu H, Yang J, Li C, Zhong Y, Tian X, Zhang M, et al. Mesoporous nanogel sprays as universal evaporation interface modifiers for boosting water-cluster evaporation. Adv Mater. 2025;37(16):e2419243. [CrossRef].
35. Wang Y, Zhang M, Chen J, Zheng P, Song X, Song Y. Bioinspired standalone 3D spacer fabric-based solar evaporator for efficient clean water production. Chem Eng J. 2025;519:165478. [CrossRef].
36. Liu H, Chen B, Chen Y, Zhou M, Tian F, Li Y, et al. Bioinspired self-standing, self-floating 3D solar evaporators breaking the trade-off between salt cycle and heat localization for continuous seawater desalination. Adv Mater. 2023;35(24):2301596. [CrossRef].
37. Liu X, Chen F, Li Y, Jiang H, Mishra DD, Yu F, et al. 3D hydrogel evaporator with vertical radiant vessels breaking the trade-off between thermal localization and salt resistance for solar desalination of high-salinity. Adv Mater. 2022;34(36):2203137. [CrossRef].
38. Nie B, Meng Y, Niu S, Gong L, Chen Y, Guo L, et al. Janus solar evaporators: A review of innovative technologies and diverse applications. Energy Environ Sci. 2025;18(8):3502–25. [CrossRef].
39. Zheng D, Shi L, Zhang M, Huang W, Li Z, Long S, et al. A self-floating and windproof Janus biomass composite hydrogel with magnetic controllability and salt rejection for polluted seawater desalination. Chem Eng J. 2024;497:154943. [CrossRef].
40. Wu M, Wei Y, Zhu Y, Bai Y, Wang Y, Wang X, et al. Hydrophilic polymer foam as a monolithic interfacial solar evaporator with rapid self-cleaning, high evaporation efficiency, and salt resistance. Adv Funct Mater. 2024;34(52):2410729. [CrossRef].
41. Jin M, Qu X, Li J, Deng L, Han Z, Chen S, et al. Bacterial cellulose-based film with self-floating hierarchical porous structure for efficient solar-driven interfacial evaporation. Carbohydr Polym. 2023;321:121324. [CrossRef].
42. Wei Z, Wang Y, Cai C, Zhang Y, Guo S, Fu Y, et al. Dual-network liquid metal hydrogel with integrated solar-driven evaporation, multi-sensory applications, and electricity generation via enhanced light absorption and Bénard–Marangoni effect. Adv Funct Mater. 2022;32(41):2206287. [CrossRef].
43. Liu G, Chen T, Xu J, Li G, Wang K. Solar evaporation for simultaneous steam and power generation. J Mater Chem A. 2020;8(2):513–31. [CrossRef].
44. Zhang Y, Hu J, Guo X, Li X, Lin J, Zhang Z, et al. Achieving solar-thermal driven dual functional device utilizing flexible PDA coated sponge integrated thermoelectric module design for water purification and power generation. Appl Surf Sci. 2024;664:160221. [CrossRef].
45. Yu Q, Wei Y, Zhang J, Wu S, Chen S, Huang Z, et al. Morning glory-inspired 3D LIG/PDA paper evaporators for efficient solar steam generation. ACS Appl Mater Interfaces. 2026;18(3):5331–43. [CrossRef].
46. Chaule S, Hwang J, Ha SJ, Kang J, Yoon JC, Jang JH. Rational design of a high performance and robust solar evaporator via 3D-printing technology. Adv Mater. 2021;33(38):2102649. [CrossRef].
47. Zhou X, Guo M, Huang M, Xu Y, Liu M. 3D printing of porous ceramic scaffold based halloysite clay for efficient seawater desalination. Chem Eng J. 2024;501:157659. [CrossRef].